Rare Metal Materials and Engineering
Volume 48, Issue 8, August 2019
Available online at www.rmme.ac.cn

Science Press

Cite this article as: Rare Metal Materials and Engineering, 2019, 48(8): 2454-2459.

ARTICLE

Grain Boundary Character Distributions of Coincidence Site Lattice Boundaries in WC-Co Composites Under Plastic Deformation

Yuan Xiaokun, Zhang Xuehong, Deng Sixu

Beijing University of Technology, Beijing 100124, China

Abstract: By virtue of five parameter analysis (FPA) method, the grain boundary character distributions (GBCDs) were measured for both Σ13*a* and Σ2 coincidence site lattice (CSL) boundaries in WC-Co composites under plastic deformation condition. For the two CSL boundaries, compared to the cases in the undeformed sample, both their populations and their habit plane occurrence frequencies decrease in the plastically deformed sample. The interpretation about the GBCD evolution during plastic deformation is proposed based on the analysis of fine-sorted crystallographic plane categories.

Key words: Σ13*a* grain boundary; Σ2 grain boundary; tungsten carbide; electron backscattered diffraction; five parameter analysis

WC-Co cemented carbide as a kind of refractory and hard material is mainly used as cutting tool material for broad industrial applications. It consists of fine particles of tungsten carbide cemented into the composite by a binder metal. Typical WC-Co cemented carbides contain 6 wt%~15 wt% cobalt as the binder phase; therefore, the properties of the material are closely related to the composition and poly-crystalline structure. There are two kinds of most-frequently-occurring WC/WC boundaries, the one can be described as a 27.796° rotation about the [0001] axis (abbreviated as 27.796°/[0001]), and the other can be described as a 90° rotation about the $[10\bar{1}0]$ axis (abbreviated as 90°/$[10\bar{1}0]$)[1]. In the coincidence site lattice (CSL) notation, the two boundaries are referred to as Σ13*a* and Σ2, respectively, and are thought to have symmetrical configurations with dense planes[2], low interfacial energies and high work of separation[3]. Particularly, for the Σ2 boundary, since the *c*/*a* ratio of WC is 0.976, it is actually an "approximate" or "near" CSL boundary.

In measuring the microstructure of polycrystals, grain boundary plane crystallography should not be neglected because the mesoscale structure of the grain boundary network can influence the integrity and performances of the material[4]. Recently, a stereological approach named "five parameter analysis (FPA)"[5] has been developed to calculate grain boundary character distribution (GBCD) from electron backscatter diffraction (EBSD) data. Using this method, the GBCD is expressed in terms of five macroscopically observable parameters, that is, three Eulerian angles describing the lattice misorientation across the boundary and two spherical angles describing the orientation of the grain boundary plane normal. Therefore, the FPA can provide a more comprehensive description of the grain boundaries within a polycrystal since it presents the information of orientation texture of boundary planes.

In addition to various cubic metals and alloys[6-8], selected hexagonal materials, including α-titanium[9,10], magnesium[11] and tungsten carbide[12], have been studied via the FPA method and their accuracy has been proved. FPA method requires extensive orientation data to reliably determine the GBCD. Because of the need for very large data sets (on the order of ten times the number of distinguishable boundaries), the previous work has not fully examined factors that can influence the distribution of CSL boundary planes[12,13] in

Received date: August 25, 2018
Foundation item: National Natural Science Foundation of China (51471007)
Corresponding author: Yuan Xiaokun, Ph. D., Senior Experimentalist, College of Materials Science and Engineering, Beijing University of Technology, Beijing 100124, P. R. China, Tel: 0086-10-67396260, E-mail: bjutfive@163.com

cemented carbides. Therefore, compared to the author's previous work[14], the objective of the current work is to more deeply compare the GBCDs for the two typical CSL boundaries (with lower and higher misorientations separately) under plastic deformation. The results would show how plastic deformation affects the population as well as the detailed GBCDs of these boundaries. To achieve this target, two samples that are nominally the same are needed, except that one should be subjected to plastic deformation to represent the load conditions when cemented carbides are used in practice.

1 Experiment

The two commercial cemented carbide sample groups used in this work are presented by the Xingyu Cemented Carbide Mould Limited Company, Zigong, China. Samples in the two groups are nominally the same, with a nominal cobalt content of 11 wt% and with no intentional alloying additions. Group 1 contains merely one specimen, namely sample 1 (similarly hereinafter), which is not deformed and is used as a reference. Group 2 contains five specimens; the reason for doing this is to avoid the impact of the contingency factors to the GBCDs during plastic deformation. For the five specimens in group 2, all of them were subjected to plastic deformation via a material test machine, MTS 810 (MTS Systems Corporation, USA) and were plastically deformed in a controlled three point bending strength test. The procedure was performed with a test span of 14.5±0.5 mm and a loading speed of 200 N/min. From these specimens, volumes of materials close to the most heavily deformed zone were extracted for further examinations. In detail, for the five specimens in group 2, their EBSD data were joined together for further GBCD analysis. We hereby refer to sample 2 (similarly hereinafter) as the joint name of the five specimens in group 2.

For EBSD analysis, all the six specimens were treated by polishing with a diamond abrasive and etching in Murakami's reagent for no more than 5 s. This treatment can yield WC surfaces suitable for EBSD mapping and can ensure the quality of the diffraction patterns. The EBSD measurements were performed by a high speed Hikiari camera (EDAX, Inc., USA) incorporated in a Quanta 250 field emission environmental scanning electron microscope (SEM, FEI Company, USA). To ensure the accuracy of the measurements, the EBSD data were collected with a step size of 0.15 μm. On each sample, more than 2×10^5 grain boundary traces were recorded to achieve an acceptable statistics for GBCD determining[5].

The microstructure and misorientation statistics represented by the boundary length fraction were derived from TSL OIM Analysis 6.2 software (EDAX Inc., USA). The Brandon criterion[15] was used to determine the fraction of CSL boundaries.

The GBCDs were calculated using programs developed at Carnegie Mellon University that contain a stereological procedure coupled with an automated trace analysis step, and the procedure for doing this is described in Ref. [5]. Using the FPA method, the GBCD, $\lambda(\Delta g, n)$, is defined as the relative area of a grain boundary with a misorientation, Δg, and boundary plane normal, n, in units of multiples of a random distribution (MRD). Note that in this work, two kinds of GBCD are measured. First, when the misorientation across the boundary plane is defined, the GBCD, $\lambda(\Delta g, n)$, is the relative area of the boundary planes with certain misorientation, that is, the occurrence frequency of typical CSL boundaries with particular misorientation relationships. Second, when the misorientations across the boundary plane are averaged, the GBCD, $\lambda(n)$, is the occurrence frequency of the habit planes. In the second case, filter codes developed by Carnegie Mellon University are used to sort the entire boundaries into $\Sigma13a$ boundaries, $\Sigma2$ boundaries and rest boundaries (that is, boundaries except $\Sigma13a$ and $\Sigma2$). The $\lambda(n)$ measurement is performed on these four boundary categories. Also note that in the current work, all the misorientation statistics are plotted via contours representing the distribution densities of the referred objects and are illustrated in units of multiples of a random distribution (abbreviated as MRD and similarly hereinafter). In these distributions, values greater than one MRD indicate the total distribution intensities associated with specific misorientations are larger than what would be expected in a random distribution, and values less than one MRD are associated with specific misorientations whose distribution intensities are less than what would be expected in a random distribution.

2 Results

The microstructure of the two samples are illustrated by the image quality (IQ) maps in Fig.1, with $\Sigma13a$ boundaries highlighted in red and $\Sigma2$ boundaries highlighted in blue. Here, the bright gray spots are the accumulated cobalt binder phase. In IQ maps, the image quality is lower for diffraction patterns obtained near grain boundaries. Both samples exhibit microstructures with a continuous skeleton of prismatic WC grains embedded in the cobalt binder phase.

The misorientation statistics represented by the boundary length fraction were measured by the following two ways. First, via a single-parameter approach (illustrating the misorientation angle), the misorientation angle distributions were calculated for the two samples and the outcomes are illustrated in Fig.2. In the chart, the black line represents the misorientation distribution for an ideally random microstructure[16] (which is fixed for subjects with hexagonal symmetries that have the same c/a ratio), while the blue and red lines show the misorientation distributions for the grain boundaries in samples 1 and 2, respectively. It can be observed that the experimental distributions are not random. Two misorientation angle preferences, corresponding to the sharp peaks at 27.796° and 90°, were observed. Furthermore, the misorientation distributions in the two samples are nearly the same, indicating that plastic deformation does not

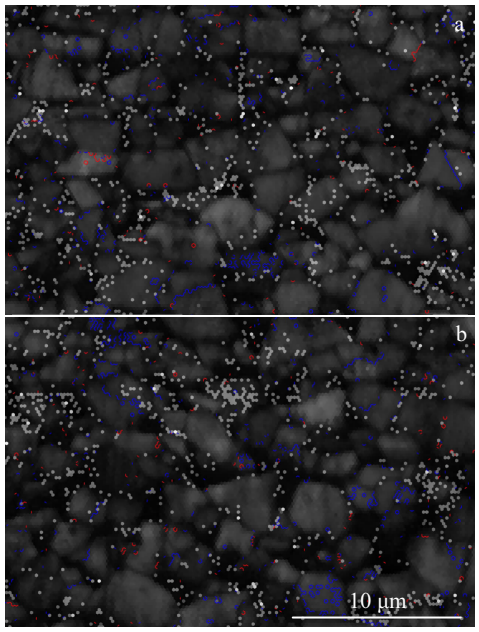

Fig.1 Image quality maps of partial and representative regions in sample 1 (a) and sample 2 (b) (Σ13*a* boundaries are highlighted in red and Σ2 boundaries are highlighted in blue. The bright gray spots are the accumulated cobalt binder phase)

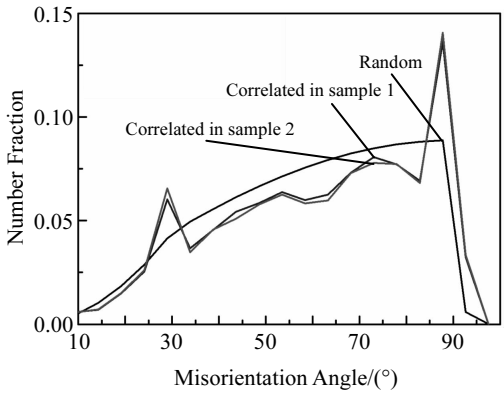

Fig.2 Grain boundary population of WC crystals and random objects as a function of misorientation angle in the two samples

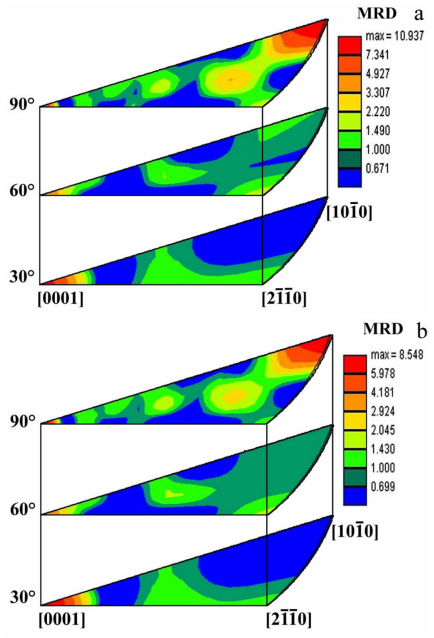

Fig.3 WC/WC grain boundary misorientation distribution in axis angle space for sample 1 (a) and sample 2 (b) (the sections of the fundamental zone are taken perpendicular to the [0001] axis)

remarkably influence the misorientation angle preferences between WC grain pairs.

Second, via a three-parameter approach (examining the distribution of misorientation axes), the EBSD data of the two samples are plotted into axis-angle space and the results are illustrated in Fig.3. In the figure, in each layer of the axis-angle space, all possible axes are represented, and the rotation angle varies along the vertical direction. Larger values indicate relatively stronger preference of that axis. As a result, for the two samples, peaks at the position of 27.796° with [0001] rotation axis can be observed, corresponding to the Σ13*a* misorientation relationship that should have high interface coincidence in the twist configuration. For the two samples, there are even larger deviations from random for 90° rotation angle at the [10$\bar{1}$0] rotation axis, corresponding to the Σ2 misorientation relationship which is the dominant misorientation. By comparing the maximum at the Σ13*a* and Σ2 positions, it can be estimated that there are about 20% reduction in the number of Σ13*a* and Σ2 boundaries. Therefore, it can be confirmed that the CSL populations are decreased as a result of plastic deformation.

The misorientation distributions in Fig.2 and Fig.3 can be used as the guide in selecting the appropriate sections for FPA analysis, that is, after a misorientation is chosen, the character distribution for that misorientation can then be plotted via a stereographic projection. As the term suggests, the FPA analysis is a five parameter case and therefore can provide more comprehensive description of boundary plane distributions. For the two samples in this work, $\lambda(\Delta g, n)$ for Σ13*a* boundaries, $\lambda(\Delta g, n)$ for Σ2 boundaries, $\lambda(n)$ for entire boundaries, $\lambda(n)$ for Σ13*a* boundaries, $\lambda(n)$ for Σ2 boundaries, and $\lambda(n)$ for rest boundaries, are illustrated in Fig.4 and Fig.5.

In Fig.4 and Fig.5, each $\lambda(\Delta g, n)$ is the relative area of grain boundary planes at the chosen misorientation. For each sample, about the $\lambda(\Delta g, n)$ for Σ13*a* boundaries (see Fig.4a and Fig.5a), the peak is at the position of the corresponding [0001] misorien-

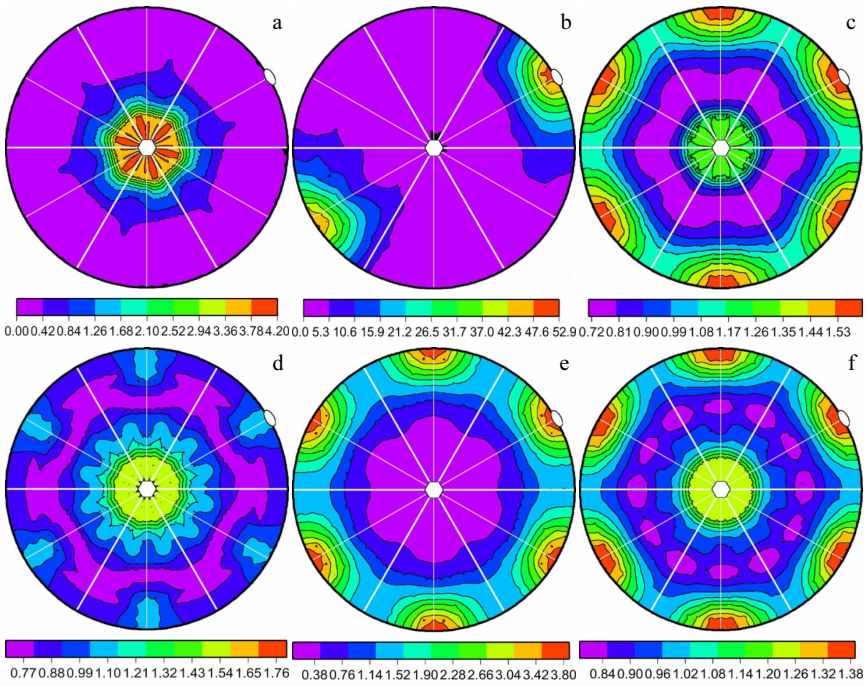

Fig.4 Grain boundary character distributions in sample 1: (a) $\lambda(\Delta g, n)$ for $\Sigma 13a$ boundaries, (b) $\lambda(\Delta g, n)$ for $\Sigma 2$ boundaries, (c) $\lambda(n)$ for entire boundaries, (d) $\lambda(n)$ for $\Sigma 13a$ boundaries, (e) $\lambda(n)$ for $\Sigma 2$ boundaries, and (f) $\lambda(n)$ for rest boundaries (the stereological approach is plotting along the [0001] direction; planes with [0001] as normal are indicated by hexagons, and planes with $[10\bar{1}0]$ as normal are indicated by ovals; contours are in units of MRD)

tation axis, meaning the boundary plane is perpendicular to the common rotation axis of the grain pair and thus is a pure twist configuration. About the $\lambda(\Delta g, n)$ for $\Sigma 2$ boundaries (see Fig.4b and Fig.5b), the peak is at the position of the corresponding $[10\bar{1}0]$ misorientation axis, meaning the boundary plane is also perpendicular to the common rotation axis of the grain pair and thus is also a pure twist configuration. MRD values in the above figures indicate that plastic deformation has reduced the populations of both $\Sigma 13a$ and $\Sigma 2$ boundaries.

In Fig.4 and Fig.5, each $\lambda(n)$ is the relative area of habit planes within a certain boundary category. For each sample, about the $\lambda(n)$ for entire boundaries (see Fig.4c and Fig.5c), the distributions of boundary plane normal have clear preferences for the (0001) and $(10\bar{1}0)$ orientations, illustrating that the (0001) and $(10\bar{1}0)$ habit planes are the most common planes; moreover, MRD values in Fig.4c and Fig.5c indicate that the plastic deformation has altered the occurring frequencies of these habit planes. About the $\lambda(n)$ for $\Sigma 13a$ boundaries (see Fig.4d and Fig.5d), both samples present obvious preference of (0001) planes, that is to say, the (0001) planes are predominant among $\Sigma 13a$ boundaries; meantime, the plastic deformation does not alter the twist configuration of $\Sigma 13a$ boundaries; moreover, MRD values in Fig.4d and Fig.5d again indicate that plastic deformation has reduced the populations of $\Sigma 13a$ boundaries. About the $\lambda(n)$ for $\Sigma 2$ boundaries (see Fig.4e and Fig.5e), both samples present obvious preference of the $(10\bar{1}0)$ planes, that is to say, the $(10\bar{1}0)$ planes are predominant among $\Sigma 2$ boundaries; meantime, the plastic deformation does not alter the twist configuration of $\Sigma 2$ boundaries; moreover, MRD values in Fig.4e and Fig.5e also indicate that plastic deformation has reduced the populations of $\Sigma 2$ boundaries. About the $\lambda(n)$ for rest boundaries (see Fig.4f and Fig.5f), it can be observed that when the CSL boundaries and their prevalent habit planes are excluded from the entire boundary population, the (0001) and $(10\bar{1}0)$ planes still are the most common planes. Since the CSL boundary populations decrease after the deformation, the relative occurrence frequency of the rest common planes increases, which can be observed from the MRD values.

3 Discussion

Considering the crystallographic structure of WC, tungsten and carbon layers are alternately arranged in an ABAB packing sequence, and the layer of small carbon atoms leads to the low c/a ratio (0.976). As the result, plastic deformation mechanisms for tungsten carbide might have specific features. In the current work, when calculated by the misorientation alone, the procedure of plastic deformation reduces the population of the $\Sigma 13a$ and the $\Sigma 2$ boundaries by a factor of 1.3 (see MRD values in Fig.3). Moreover, the FPA analysis outcomes indicate that the plastic deformation has reduced the population of the $\Sigma 13a$ and the $\Sigma 2$ boundaries by a factor of 1.8 (see MRD values in Fig.4a

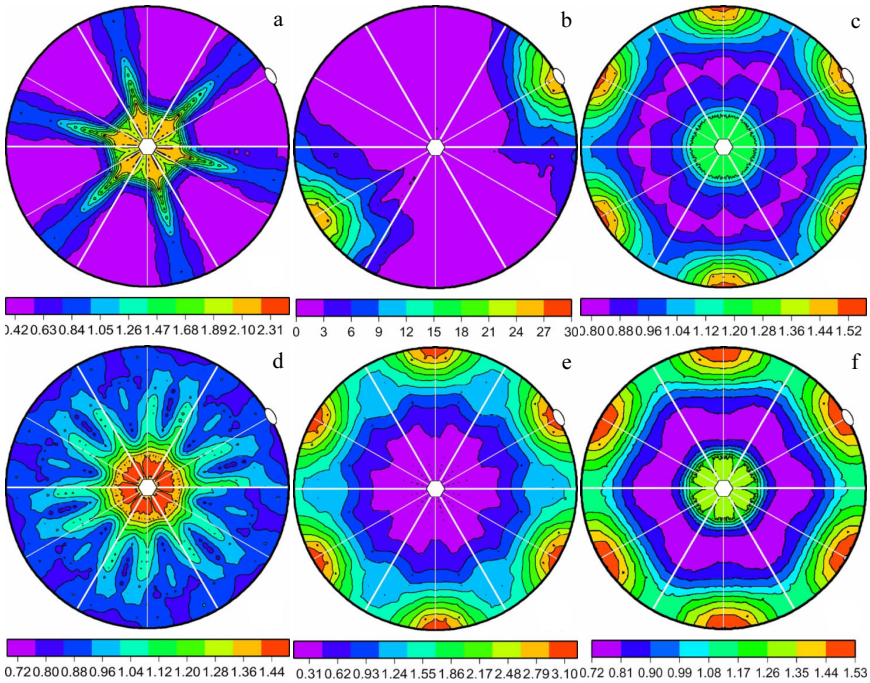

Fig.5 Grain boundary character distribution in sample 2: (a) $\lambda(\Delta g, n)$ for $\Sigma 13a$ boundaries, (b) $\lambda(\Delta g, n)$ for $\Sigma 2$ boundaries, (c) $\lambda(n)$ for entire boundaries, (d) $\lambda(n)$ for $\Sigma 13a$ boundaries, (e) $\lambda(n)$ for $\Sigma 2$ boundaries, and (f) $\lambda(n)$ for rest boundaries (the stereological approach is plotting along the [0001] direction; planes with [0001] as normal are indicated by hexagons, and planes with $[10\bar{1}0]$ as normal are indicated by ovals; contours are in units of MRD)

and Fig.5a for $\Sigma 13a$ boundaries, and MRD values in Fig.4b and Fig.5b for $\Sigma 2$ boundaries). The above results remind us that slip systems (including basal, prismatic and pyramidal approaches) should be mainly concerned in analyzing the GBCDs in this work. Meantime, certain details should also be focused; most importantly, for partial WC/WC grain pairs, their grain boundary planes are rotated while their misorientations are maintained.

As to the $\lambda(\Delta g, n)$ for $\Sigma 13a$ boundaries (see Fig.4a and Fig.5a), the alteration of GBCD most likely origins from the (0001) grain boundary sliding: sliding parallel to the basal plane would reduce the total area of $\Sigma 13a$ boundaries by reducing the total area of contact. Nevertheless, it should be noted that although the (0001) basal plane has a high packing density, the basal slip relatively less occurs since strong bond forces between carbon and tungsten atoms across the ABAB layers prevent shearing along directions in the basal plane[17].

As to the $\lambda(\Delta g, n)$ for $\Sigma 2$ boundaries (see Fig.4b and Fig.5b), since the twist configuration of $\Sigma 2$ boundaries is maintained during plastic deformation, the alteration of GBCD can thus be mainly attributed to the grain boundary sliding that parallel to the $(10\bar{1}0)$ grain boundary plane, and such mechanism is thought to be an important deformation approach in cemented carbides[18,19]; moreover, such sliding mechanism could be facilitated when the WC skeleton breaks up and grain boundaries are infiltrated by the Co binder phase[3]. However, the lower interface energy of $\Sigma 2$ twist boundary[20] means that the $\Sigma 2$ twist boundary is relatively difficult to be separated and then be infiltrated by the binder. For the grain pairs with rotated boundary plane and maintained misorientation, a mechanism considering grain shape changes associated with dislocation motion has been proposed in the author's previous work[14], which suggests the possible cross slip of screw dislocations along $\{10\bar{1}0\}$ planes based on the $<0001>\{10\bar{1}0\}$ slip system[19].

The alteration of the GBCDs of typical CSL boundaries can reduce the contact area of both (0001) and $(10\bar{1}0)$ planes, and can also lead to the reorientation of boundary planes to some extent. Therefore, the $\lambda(n)$ studies of various boundary categories provide an alternative to check the distribution features of habit planes during plastic deformation. As to the $\lambda(n)$ for entire boundaries (see Fig.4c and Fig.5c), the (0001) basal and $(10\bar{1}0)$ prismatic planes remain as the most prevalent crystallographic planes after plastic deformation, and the population of such habit planes is not significantly changed by the plastic deformation. As to the $\lambda(n)$ for $\Sigma 13a$ boundaries (see Fig.4d and Fig.5d), the twist structure of $\Sigma 13a$ boundaries can be proved, that is, the (0001) basal planes occupy predominant fractions among the $\Sigma 13a$ boundary planes, and the twist boundary (consists of (0001) planes on the two sides) is the most common configuration. Meantime, lower MRD value of (0001) planes after plastic deformation can help to suggest the

(0001) grain boundary sliding mechanism. As to the $\lambda(n)$ for Σ2 boundaries (see Fig.4e and Fig.5e), the twist feature of Σ2 boundaries can be proved, and the $(10\bar{1}0)$ prismatic planes (as predominant planes) consist the crystallographic planes on the two sides of the Σ2 twist boundaries. Moreover, lower MRD value of $(10\bar{1}0)$ planes after plastic deformation might be attributed to the $(10\bar{1}0)$ prismatic sliding mechanism; it might also be attributed to the cross slip of dislocations through the interface plane. As to the $\lambda(n)$ for rest boundaries (see Fig.4f and Fig.5f), the (0001) and $(10\bar{1}0)$ planes keep as the representative habit planes among common boundaries, and since the population of CSL boundaries decreases after plastic deformation, the population of these common boundaries increases accordingly.

4 Conclusions

Comparisons of GBCDs in the un-deformed and plastically deformed WC-Co samples via the FPA method lead to the following conclusions: for the Σ13*a* and Σ2 CSL boundaries, their population decreases while their twist configurations are remained during plastic deformation. The deformation procedure does not significantly change the fraction of CSL misorientations; however, it alters the fraction of twist CSL boundaries more obviously. The phenomena can mainly be attributed to the basal and prismatic slip system, and to some extent, can be attributed to the reorientation of carbide grains via the cross slip of dislocations.

References

1 Hagége S, Nouet G, Delavignette P. *Physica Status Solidi*[J], 1980, 62(1): 97
2 Vicens J, Benjdir M, Nouet G *et al*. *Journal of Materials Science*[J], 1994, 29(4): 987
3 Christensen M, Wahnstrom G. *Physical Review B*[J], 2003, 67(11): 115 415
4 Rohrer G S. *Journal of the American Ceramic Society*[J], 2011, 94(3): 633
5 Saylor D M, El-Dasher B S, Adams B L *et al*. *Metallurgical and Materials Transactions A*[J], 2004, 35(7): 1981
6 Ratanaphan S, Olmsted D L, Bulatov V V *et al*. A*cta Materialia*[J], 2015, 88: 346
7 Zhong X T, Rowenhorst D J, Beladi H *et al*. *Acta Materialia*[J], 2017, 123: 136
8 Beladi H, Tari V, Timokhina I B *et al*. *Acta Materialia*[J], 2017, 127: 426
9 Beladi H, Chao Q, Rohrer G S. *Acta Materialia*[J], 2014, 80: 478
10 Kelly M N, Glowinski K, Nuhfer N T *et al*. *Acta Materialia*[J], 2016, 111: 22
11 Ostapovets A, Molnar P, Lejcek P. *Materials Letters*[J], 2014, 137: 102
12 Kim C S, Massa T R, Rohrer G S. *Journal of the American Ceramic Society*[J], 2008, 91(3): 996
13 Kim C S, Rohrer G S. *Interface Science*[J], 2004, 12(1): 19
14 Yuan X K, Rohrer G S, Song X Y *et al*. *International Journal of Refractory Metals and Hard Materials*[J], 2014, 47: 38
15 Brandon D G. *Acta Metallurgica*[J], 1966, 14(11): 1479
16 Mackenzie J K. *Biometrika*[J], 1958, 45(1-2): 229
17 Bolton J D, Redington M. *Journal of Materials Science*[J], 1980, 15(12): 3150
18 Petisme M V G, Gren M A, Wahnstrom G. *International Journal of Refractory Metals and Hard Materials*[J], 2015, 49: 75
19 Johansson S A E, Petisme M V G, Wahnström G. *Computational Materials Science*[J], 2015, 98: 345
20 Östberg G, Farooq M U, Christensen M *et al*. *Materials Science and Engineering A*[J], 2006, 416(1-2): 119

塑性变形条件下硬质合金中重位点阵晶界的特征分布

原效坤，张雪红，邓思旭

(北京工业大学，北京 100124)

摘　要：通过五参数法，测定了一种塑性变形条件下硬质合金结构中的两类重位点阵晶界，即 Σ13*a* 晶界和 Σ2 晶界的晶界特征分布。通过与未经过塑性变形的试样进行对比，发现两类重位点阵晶界的数量以及相应惯习面的赋存频率，在塑性变形条件下都有所降低。通过对硬质合金试样结构中的晶界面类型进行精确区分，塑性变形条件下晶界特征分布的演进过程得到解释。

关键词：Σ13*a* 晶界；Σ2 晶界；硬质合金；电子背散射衍射；五参数法

作者简介：原效坤，男，1974 年生，博士，高级实验师，北京工业大学材料科学与工程学院，北京 100124，电话：010-67396260，E-mail: bjutfive@163.com